

Superabsorbing, Artificial Metal Films Constructed from Semiconductor Nanoantennas

Soo Jin Kim,[†] Junghyun Park,[†] Majid Esfandyarpour,[†] Emanuele F. Pecora,[†] Pieter G. Kik,^{†,‡} and Mark L. Brongersma^{*,†}

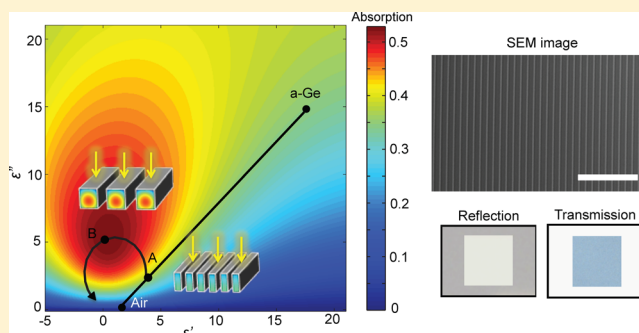
[†]Geballe Laboratory for Advanced Materials, 476 Lomita Mall, Stanford, California 94305-4045, United States

[‡]CREOL, The College of Optics and Photonics, University of Central Florida, 4000 Central Florida Boulevard, Orlando, Florida 32816, United States

S Supporting Information

ABSTRACT: In 1934, Wilhelm Woltersdorff demonstrated that the absorption of light in an ultrathin, freestanding film is fundamentally limited to 50%. He concluded that reaching this limit would require a film with a real-valued sheet resistance that is exactly equal to $R = \eta/2 \approx 188.5 \Omega/\square$, where $\eta = \sqrt{\mu_0/\epsilon_0}$ is the impedance of free space. This condition can be closely approximated over a wide frequency range in metals that feature a large imaginary relative permittivity ϵ_r'' , that is, a real-valued conductivity $\sigma = \epsilon_0 \epsilon_r'' \omega$. A thin, continuous sheet of semiconductor material does not facilitate such strong absorption as its complex-valued permittivity with both large real and imaginary components preclude effective impedance matching. In this work, we show how a semiconductor metafilm constructed from optically resonant semiconductor nanostructures can be created whose optical response mimics that of a metallic sheet. For this reason, the fundamental absorption limit mentioned above can also be reached with semiconductor materials, opening up new opportunities for the design of ultrathin optoelectronic and light harvesting devices.

KEYWORDS: Metafilm, Mie resonance, germanium nanobeam, semiconductor nanoantenna, light absorption



The achievement of very strong light-matter interaction in ultrathin semiconductor layers is key to realizing next-generation optoelectronic applications. Thinner devices are more lightweight, flexible, and offer advantages in terms of reduced materials and processing cost. Shrinking device dimensions can also result in an improved performance. For example, achieving strong light absorption in increasingly thin semiconductor layers will naturally result in increases in the speed and efficiency of photocarrier extraction. This finds application in a wide variety of technologies, including solar energy harvesting,^{1–4} photodetectors,^{5,6} and thermal photovoltaics.^{7,8}

From the early 1900s, researchers have been eager to understand the ultimate limits to absorption of electromagnetic waves in layers of material that are much thinner than the wavelength λ of the incident radiation. Woltersdorff,⁹ Dallenbach,¹⁰ and Salisbury^{11–13} explored these limits for thin metal and lossy dielectric films with and without backreflectors. Here, we aim to understand the maximum absorption one can achieve in a subwavelength layer of semiconductor material deposited on a transparent substrate. As a starting reference point, it is of value to note that the absorption limit of an ultrathin ($t \ll \lambda$) free-standing film in air

is exact 50%. Unity absorption can only be reached with the aid of back reflector.^{12,13}

In order to reach the 50% limit, Woltersdorff concluded that the film needs to be a metal with a purely real-valued sheet resistance of $R = \eta/2 \approx 188.5 \Omega/\square$, where $\eta = \sqrt{\mu_0/\epsilon_0}$ is the impedance of free space. This facilitates the best possible impedance match of a homogeneous thin film to its environment, minimizing the reflected and transmitted power (Supporting Information S1).^{14,15} This conclusion could have been reached by creating a map of the light absorption versus the real and imaginary parts of the relative permittivity ϵ' and ϵ'' . Figure 1a shows such a map for a free-standing, 40 nm thick film at the wavelength of 600 nm in the visible range. It can be observed that the maximum absorption occurs when ϵ' is small compared to ϵ'' , which happens for a relative permittivity of $\hat{\epsilon}_r = 0.436 + i5.35$. The absorption is slightly above 50% ($\sim 52.9\%$), which is possible due to a very small phase shift due to the propagation through the film. This is equivalent to the statement that the dielectric loss tangent, defined as the

Received: March 21, 2016

Revised: April 26, 2016

Published: May 5, 2016

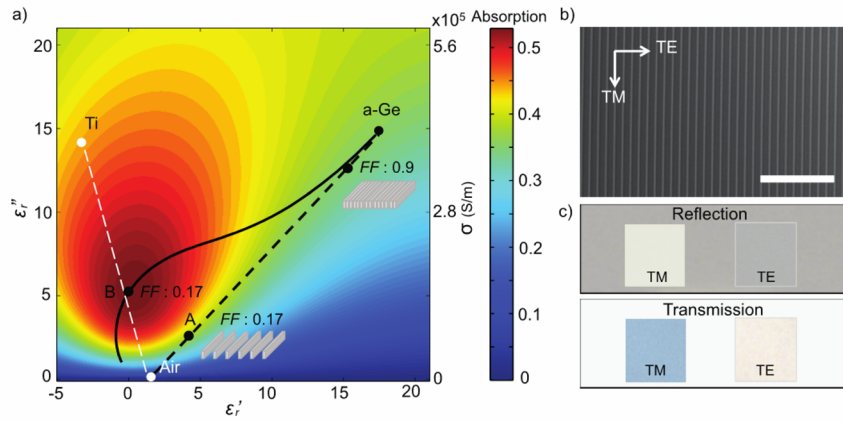


Figure 1. Optimization of the light absorption in a thin free-standing film. (a) Absorption map of a thin, free-standing film as a function of its optical properties. The film is chosen to be 40 nm thick and the illumination wavelength is 600 nm. Dashed lines represent the achievable effective optical constants with metafilms of different compositions (white, Ti/Air; black, Ge/Air) and as obtained by first-order effective medium theory. The black solid line shows the achievable effective optical constants of a metafilm composed of 50 nm wide, resonant Ge nanobeams and air. Point A and B are the optical constants with a Ge filling fraction of 0.17. (b) SEM image of a fabricated metafilm constructed from an array of 50 nm-wide, resonant Ge nanobeams on a quartz substrate. The scale bar is 2.7 μm . (c) Optical images of polarized white light reflection (top) and transmission (bottom) for structures aligned along (TM) and normal (TE) to the incident polarization. The reflection and transmission of the quartz substrate can be seen in the unpatterned area surrounding the metafilm regions.

ratio of the imaginary and real part of the permittivity $\tan \delta = \epsilon''/\epsilon'$ needs to be large. This general requirement holds true for all film thicknesses $t \ll \lambda$ (see Supporting Information S1) and can be understood from an expression of the time-averaged power dissipation density associated with the material polarization at a certain angular frequency ω

$$\begin{aligned} \langle P_d \rangle &= \left\langle \frac{\mathbf{E} \cdot \partial \mathbf{D}}{\partial t} \right\rangle = 0.5 \text{Re} \{ -i\omega \hat{\mathbf{D}} \cdot \hat{\mathbf{E}}^* \} \\ &= 0.5 \text{Re} \{ -i\omega \epsilon_0 (\epsilon_r' + i\epsilon_r'') \hat{\mathbf{E}} \cdot \hat{\mathbf{E}}^* \} = 0.5 \omega \epsilon_0 \epsilon_r'' |\hat{\mathbf{E}}|^2 \tan \delta \end{aligned}$$

where boldface denotes a vector quantity and the “ \wedge ” symbol denotes a complex quantity.¹⁶ In this expression and for the rest of the paper, an $e^{-i\omega t}$ time-harmonic dependence is assumed. The dissipation is governed by the dot product of the electric field \mathbf{E} and displacement current density $\partial \mathbf{D}/\partial t$, much like the Ohmic dissipation in metals is linked to the dot product of the electric field and the current density of mobile charges $\langle P_d \rangle = \langle \mathbf{E} \cdot \mathbf{J} \rangle$. The magnitude of δ is a phase angle that quantifies how much the electric displacement lags the driving electric field

$$\hat{\mathbf{D}} = \epsilon_0 (\epsilon_r' + i\epsilon_r'') \hat{\mathbf{E}} = \epsilon_0 \hat{\epsilon}_r |e^{i\delta} \hat{\mathbf{E}}$$

From this brief analysis, the critical role δ plays in determining the optical loss is clear. The highest dissipation occurs when $\delta = 90^\circ$ and the displacement current is in phase with the electric field. For this value of δ , the oscillating current produces a scattered wave with a field that is perfectly out of phase with the field of the transmitted wave, facilitating its best possible cancellation of the forward wave (see Supporting Information S1). The strength of the dissipation in a lossy dielectric and conventional metal can quantitatively be compared by realizing that $\epsilon'' = \sigma/\omega\epsilon_0$, which links the ability to drive displacement and real currents. It is thus clear that the requirement for a real-valued sheet resistance of a metal is equivalent to the requirement for a high loss tangent in a dielectric.

The next important question to address is how a high loss tangent can be reached with semiconductors. Typical semiconductors, such as germanium in our example, have high values of both ϵ' and ϵ'' (see Figure 1a) and this precludes

good impedance matching using a homogeneous semiconductor film. In the hopes of changing the situation, one can leverage metamaterials, artificially designed materials whose optical properties can be tuned by nanostructuring.^{17–20} We start by considering a very simple metamaterial design consisting of a dense array of deep-subwavelength rectangular nanobeams. Normally incident light can be classified as a transverse magnetic (TM) excitation with the electric field along the nanobeams or a transverse electric (TE) excitation with the electric field in the orthogonal direction. For TM polarization, the effective permittivity is simply determined by the optical properties of the two constituent materials ($\hat{\epsilon}_1$ and $\hat{\epsilon}_2$) and their relative filling fraction (f_1 and $f_2 = 1 - f_1$) as $\hat{\epsilon}_{\text{eff}} = f_1 \hat{\epsilon}_1 + (1 - f_1) \hat{\epsilon}_2$.^{21–23} Within this approximation that is valid when the structural dimensions are much smaller than the wavelength of light, the absolute size of the beams is irrelevant. Metals naturally feature a large conductivity and loss tangent. For this reason, it is straightforward to design a strongly absorbing metafilm with metal beams surrounded by air. As an example, the white dashed line in Figure 1a displays the achievable effective permittivities for varying filling fractions of a 40 nm thick titanium (Ti) metafilm, created by removing metal to create a periodic, deep-subwavelength beam array. The thickness of 40 nm was chosen somewhat arbitrarily as one that is very thin compared to the freespace wavelength of light in the visible spectral range (400–700 nm). However, the following analysis could be made for any film with a deep subwavelength thickness. A filling fraction of 0.34 metal and 0.66 air results in a permittivity approximately equal to the targeted relative permittivity value for which the absorption is maximized. Several works have demonstrated the ultimate absorption limit of 50% with nanostructured metallic films.^{24,25} Furthermore, near-unity absorption has been attained with a back reflector behind the absorbing layer.^{7,12,13,26,27} On the other hand, both the real and imaginary parts of the permittivity of semiconductors are positive in nature, and the desired optical properties for maximum absorption cannot be reached. As an example, the black dashed line depicts the achievable effective permittivities for a 40 nm-thick (same as before) metafilm

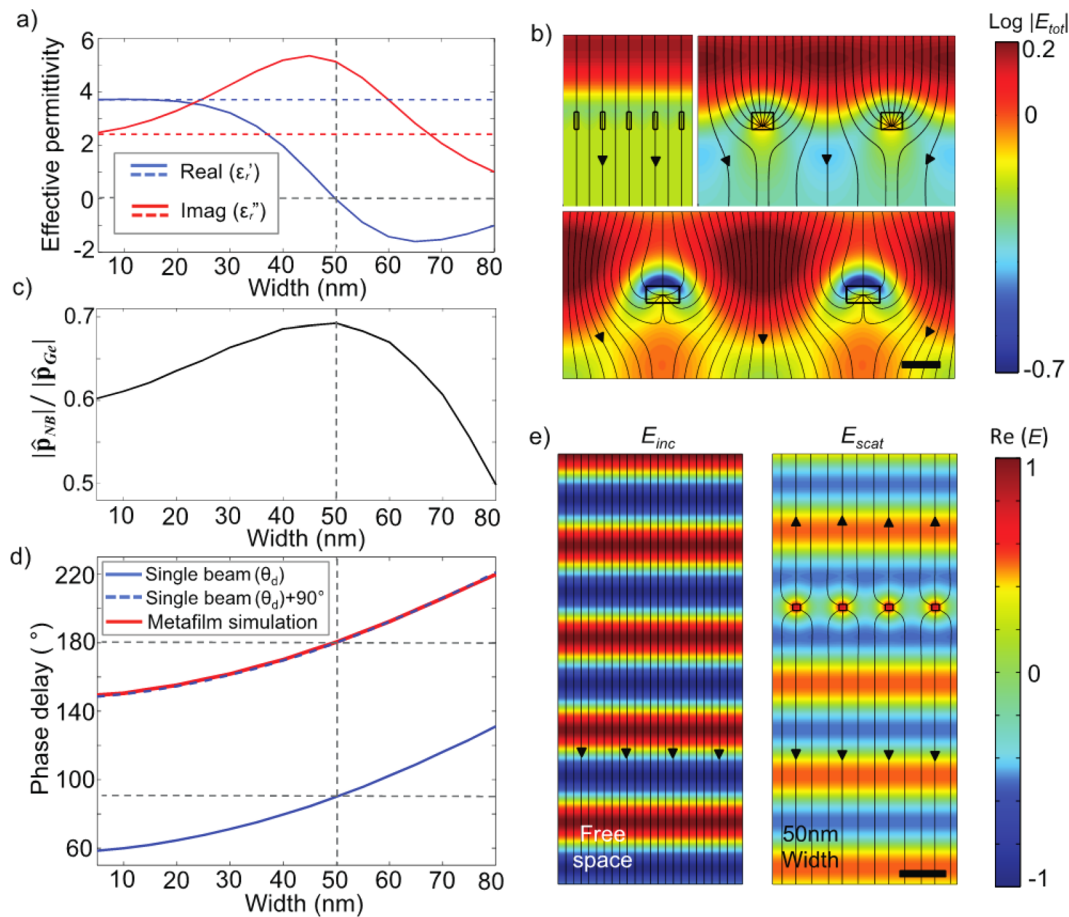


Figure 2. Evolution of the optical properties of a semiconductor metafilm from semiconductor-like to metal-like under TM illumination. (a) Changes in the effective optical properties of a 40 nm thick Ge metafilm upon changing the width of the constituent nanobeams. The probe wavelength was chosen to be 600 nm and the filling fraction of Ge beam-material was fixed at 0.17. The blue and red lines represent the real and imaginary parts of the permittivity. Dashed blue and red lines represent the values of effective index based on first order effective medium theory. (b) Maps of the total field distributions and power flow for top-illuminated metafilms with Ge nanobeams of 10 nm width (upper left), 50 nm width (top right), and 80 nm width (bottom). The scale bar for these images is 80 nm. (c) Magnitude of the dipole moment of a resonant nanobeam versus the beam width. The dipole moment of the beam is normalized by the magnitude of the dipole moment the Ge beam were to have if it were polarized by the incident field. (d) Changes in the phase delay of the forward-scattered wave with respect to the incident wave upon changing the Ge beam width. The case for a single beam (blue line), an estimate for an array of beams from individual beam properties (blue dotted line), and full field simulation (red) are shown. (e) Maps of the incident and scattered field profiles for a top-illuminated metafilm with 50 nm wide nanobeams. The scale bar is 300 nm.

constructed from an array of Ge beams with deep subwavelength dimensions. At no Ge filling fraction is 50% absorption reached. Therefore, it seems to be impossible to make the Ge–air structure act as a metallic film with a large loss tangent. Interestingly, the reverse case has been demonstrated and researched extensively. Here, a thin metal film was patterned at a subwavelength scale to make it optically look like an artificial dielectric with a high-magnitude and real-valued permittivity.^{28,29} As such, one may wonder whether a judiciously nanopatterned semiconductor film can be made to act optically as a thin metal layer.

Next, we demonstrate that Ge metafilms constructed from properly designed nanobeams that support optical resonances can in fact behave like metals and reach the 50% absorption limit. High-index semiconductor nanobeams with sizes as small as 10 nm and different cross-sectional shapes can exhibit Mie-like optical resonances by which light is trapped and concentrated inside the nanostructure.^{30,31} The first-order effective medium theory is incapable of taking into account the impact of such optical resonances on the effective optical

properties. The redistribution of the fields resulting from the excitation of resonant modes requires full-field simulations or higher-order effective medium theories. The effective optical properties of a nanostructured film can be extracted from full-field simulations using standard procedures in which the transmission and reflection properties of the film are quantified.^{32,33} By comparing results from the first-order theory and full-field simulations, the impact of resonances on the optical properties can be analyzed. For example, the achievable effective permittivities for a 40 nm thick metafilm constructed from an array of 50 nm wide Ge nanobeams follow the black solid line in Figure 1a. This trajectory of achievable permittivity values deviates significantly from the linear trajectory for the metafilm constructed from very deep-subwavelength building blocks (for which the lowest-order effective medium theory holds) and moves right through the center of the high absorption region. At a filling fraction of 0.17 (point B), the loss tangent is very high ($\tan\delta = 520$) and the film optically performs very similarly to an ideal conductor with the optimal conductivity of $\sigma = 1.4 \times 10^5$ S/m. At this point, the absorption

limit of 50% is reached. Figure 1b shows a scanning electron microscopy (SEM) image of such a metafilm on a quartz substrate patterned by electron beam lithography (see Methods).

Figure 1c shows linearly polarized optical reflection and transmission images taken from fabricated sample of a Ge metafilm with its geometrical parameters chosen as above to maximize absorption at a wavelength of 600 nm. It shows two square regions in which the Ge beams are oriented in two orthogonal directions such that the polarization of the illumination is effectively in the TM (left panel) or TE direction (right panel). The background shows the reflection from the quartz substrate that features a very high, near-unity transmission of $\sim 92\%$. The appearance of the resonant metafilm under TM illumination is much brighter in reflection and darker in transmission due to the strong, resonant light-matter interaction in the nanobeams that make up the metafilm. On the other hand, under TE illumination the film and surroundings appear similar. This results from the fact that the 50 nm wide beams are too small to support a resonant mode in the visible spectral range for this polarization. For this reason, the effective optical properties of the film nicely follow the first order effective medium theory, and an index $\hat{n} = 1.09 + 0.003i$ close to that of air as found from simulations (see Supporting Information S2).

To better understand the difference between metafilms made from resonant and nonresonant building blocks, we investigate how the effective optical properties under TM illumination evolve as the widths of the constituent Ge beams are gradually increased. In Figure 2, we analyze this evolution again at the illumination wavelength of 600 nm and a film thickness of 40 nm surrounded by air on both sides. We keep the Ge filling fraction fixed to 0.17, implying that an increase in the beam width comes with an increase in the period. By using a fixed filling fraction, we can directly quantify how the resonance impacts the optical properties, as for a nonresonant system the complex permittivity values would remain constant at a fixed filling fraction. Whereas the effective permittivity based on first order effective medium theory remains constant at $\hat{\epsilon}_{\text{eff}} = 3.7 + 2.4i$ (dashed lines), the extracted parameters from full-field simulations show an evolution as depicted by the solid lines in Figure 2a. For very narrow beam widths, the permittivity extracted from full-field simulations converges to the values obtained from the first-order effective medium theory. However, as the beam width is increased, the impact of the resonance is to reduce the real part of the relative permittivity (blue), ultimately causing its magnitude to drop below zero at a width of 50 nm. At the same time, the imaginary part of the permittivity is increased, reaching a maximum value near this same width. At this width the beams are on resonance at the considered wavelength of 600 nm. For larger widths, the complex permittivity values further evolve as one moves beyond the resonance. The graph is cut off for larger widths as these have corresponding magnitudes of the period at which diffracted orders are produced in the glass substrate and a metamaterials picture becomes untenable.

The presence of optical resonances in the nanobeams can also be seen in the optical electric field profile and the stream lines of the power flow (Poynting vector field) for a TM light wave that is normally incident on a metafilm. Figure 2b shows these quantities for three representative metafilms with beam widths of 10, 50, and 80 nm. When the beam widths are 10 nm, they are too small to support an optical resonance and most of

light flows through the film undisturbed, that is, without altering its direction. For the case of 50 nm wide beams, the beams are on resonance and the incident light is effectively funneled into the beams due to an optical antenna effect.³⁴ The 80 nm beams are too wide to be on resonance and a significant amount of light again flows past the nanobeams.

Figure 2c,d analyzes how the effective optical properties of the homogenized Ge metafilm emerge from the optical properties of the constituent nanobeams. These figures show the amplitude and phase of the scattered field of the individual beams in the metafilm. Figure 2b illustrates how the resonant excitation of the nanobeams under TM polarization can produce a very simple electric field distribution with one antinode inside the nanobeam. This field induces a displacement current along the direction of the driving electric field. The current in turn produces a scattered field that mimics that of a linear electric dipole in the far-field. As such, the beams can be treated as electrical dipole resonators with a complex polarizability $\hat{\alpha}_{\text{NB}} = |\hat{\alpha}_{\text{NB}}|e^{i\theta_d}$, where θ_d is the phase lag between the electric dipole moment created in the wire and the electric field that excites it. The dipole moment of the nanobeam can be evaluated from the full-field simulations as shown in Figure 2b by integrating the polarization vector of the nanobeam volume V_{NB} as

$$\hat{\mathbf{p}}_{\text{NB}} = \int_{\text{NB}} \hat{\mathbf{P}}(\mathbf{r}') d\mathbf{r}' = \epsilon_0 \hat{\chi}_{\text{Ge}} \int_{\text{NB}} \hat{\mathbf{E}}(\mathbf{r}') d\mathbf{r}'$$

where $\hat{\chi}_{\text{Ge}}$ is the susceptibility of Ge. To get a sense for how the resonance impacts the magnitude of this dipole moment, we normalize this quantity by another dipole moment $\hat{\mathbf{p}}_{\text{Ge}} = \epsilon_0 \hat{\chi}_{\text{Ge}} \hat{\mathbf{E}}_{\text{Inc}} V_{\text{NB}}$. This is the dipole moment that would be achieved if the Ge nanobeam were polarized by the (nonresonantly enhanced) incident field $\hat{\mathbf{E}}_{\text{Inc}}$ illuminating the nanobeam. Figure 2c shows that the magnitude of the dipole moment reaches a maximum for a beam width of 50 nm. At this wavelength, the beams of this width are driven on resonance. Interestingly, the magnitude of the dipole moment does not increase very much by virtue of having a resonance in the beam. We can thus make the important observation that for highly polarizable materials such as Ge, it is not critical to use a resonance to boost the magnitude of the dipole moment to achieve strong absorption.³⁵ Instead, we will show that the critical role of the resonance is to delay the scattered waves with respect to the incident wave.

The solid blue line in Figure 2d shows that the phase of the scattered field also progresses as the width of the nanobeams is increased from below to above the resonant beam width. On resonance, the scattered fields feature a phase lag of exactly 90° . This is in agreement with the famous Lorentz (i.e., mass-spring) model for optical resonators, which teaches us that the phase lag progresses from 0 to 180° in moving spectrally through a resonance.³⁶ This is related to the fact that at low frequencies the displacement of the bound charges can follow the driving fields and at frequencies above the resonance frequency they lose this ability. The nonzero phase lag at very small beam widths is related to the finite height (40 nm) of the nanobeams.

For the metafilm, the scattered waves generated by each of the individual nanobeam-resonators interfere to produce a forward-scattered wave on the transmission side. The coherent addition of the scattered fields from all of the individual beams in the plane of the film produce a forward-scattered wave with a 90° phase lag relative to the scattered field emerging from the

individual beams.³⁶ In the direction of propagation, the forward-scattered wave and the incident wave combine to produce the transmitted wave with a total field^{36,37}

$$\hat{\mathbf{E}}_{\text{tot}} = \hat{\mathbf{E}}_{\text{inc}} + i\hat{\mathbf{E}}_{\text{scat}} \cdot e^{i\theta_{\text{film}}}, \text{ where } \theta_{\text{film}} = \theta_d + \frac{\pi}{2} = \tan^{-1} \frac{\alpha_{\text{NB}}''}{\alpha_{\text{NB}}'} + \frac{\pi}{2}$$

Here, $\hat{\mathbf{E}}_{\text{scat}}$ is the field of the forward-scattered waves, θ_{film} denotes the phase delay of the field of the forward-scattered wave. The blue dotted line in Figure 2d shows the progression of θ_{film} as calculated by adding $\pi/2$ to the phase calculated for the individual nanobeam resonators in the film. The red line is the phase delay for the metafilm as calculated by full-field simulations. The red and blue dotted lines show a good quantitative agreement. It is thus clear that knowledge of the resonant properties of the individual beam can be very helpful for the design of a resonant metafilm and understanding its operation. The effective permittivities at 600 nm for the metafilms with 10 and 50 nm beams correspond to the points A and B in Figure 1a. The evolutionary resonant curve in Figure 2a shows how the permittivity is transformed from A to B. The loss angle δ ($= \tan^{-1} [\epsilon''/\epsilon']$) changes from approximately 39° to 90° in going from point A to B. It can be seen that moving from nonresonant to resonant beams can be thought of as a rotation in the complex permittivity plane.

Figure 2e visualizes the phase delay of the scattered optical field for the beam width of 50 nm by making a comparison to the incident field, which serves as a useful reference. As the nanobeam width is increased from 10 nm, the scattered waves reradiated from the array are increasingly delayed with respect to the incident wave. For the width of 50 nm, the phase of the forward-scattered wave is exactly π -delayed and the magnitude of the field of the forward-scattered wave equals half of the magnitude of incident field. At this optimal condition, the forward-scattered wave achieves the maximum possible destructive interference with the incident wave on the transmission side of the metafilm. At this point, 25% of the light is transmitted and 25% is reflected. This situation is exactly the same as the case of a metallic thin film with an optimized conductivity.

Next, we experimentally demonstrate the above concepts with the help of reflectivity and transmissivity measurements on a judiciously designed metafilm constructed from resonant building blocks. By lithographic means, a series of 40 nm-thick-metafilms with 50 nm-wide-Ge beams were patterned on a quartz (c-SiO₂) substrate (see Method for fabrication steps). The array periods were varied from 500 to 250 nm. The array period is a critical parameter as it controls whether first order diffraction can occur in the SiO₂ substrate or not. The occurrence of diffracted orders by definition precludes a description of the array as a metamaterial with homogenized optical properties. This point is illustrated in Figure 3a, which shows a schematic of the nanobeam array on a quartz substrate with the reflected and possible transmitted channel of interests. For periods that are subwavelength ($P < \lambda/n_{\text{SiO}_2}$), only the zeroth-order propagates on the transmission and reflection sides. On the other hand, for periods larger than the wavelength of light in the substrate, higher-order diffraction channels open up by which the light can leave the film surface. Whereas the simulated optical field for an illumination wavelength of 600 nm and a 500 nm period show diffraction into three different orders (Figure 3b), for 300 nm periods only the zeroth order is transmitted (Figure 3c). In the latter case, a description of the metafilm in terms of effective optical properties can be helpful.

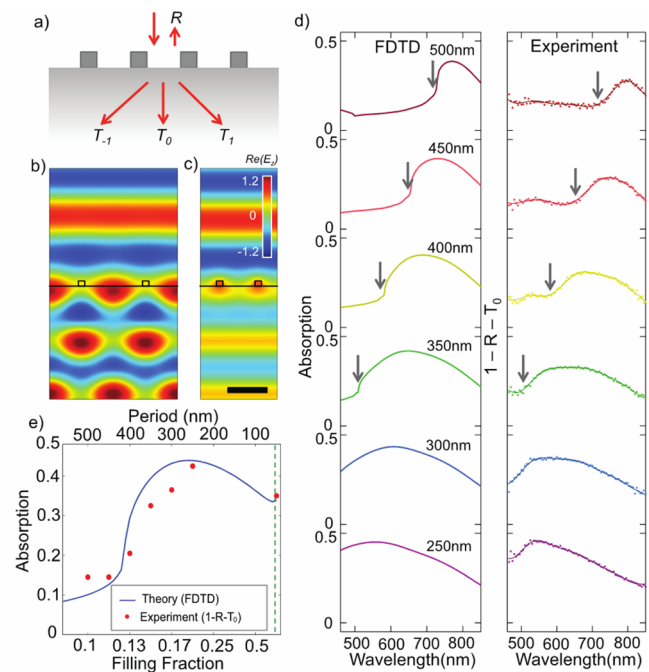


Figure 3. Experimental and simulated estimates of the absorption by designer Ge metafilms. (a) Schematic of a top-illuminated Ge metafilm on a quartz substrate showing the possible reflected and transmitted channel of interests. (b,c) Optical electric field profile at an illumination wavelength of $\lambda = 600$ nm and for the beam periods of 500 nm (b) and 300 nm (c). The scale bar is 300 nm. (d) Simulated (left panel) and experimental (right panel) absorption spectra of the fabricated Ge metafilms with different periods labeled from 500 to 250 nm from top to bottom. The vertical arrows indicate the spectral locations at which $\lambda/n_{\text{SiO}_2} = P$, where the first diffraction-order channels open up in transmission. (e) Absorption at $\lambda = 600$ nm in the Ge metafilms with different filling fractions/periodicities as extracted from in panel d. The blue line provides the simulated absorption and the red dots provide experimental values of the absorption as estimated from reflectivity and transmissivity measurements as $A = 1 - R - T_0$. The vertical green dashed line indicates the period/filling fraction for a continuous film.

In this regime one can also conveniently estimate the absorptivity A in the film through measurements of the film's reflectivity R and transmissivity T_0 into the zeroth-order as $A = 1 - R - T_0$.

The left panel in Figure 3d shows simulated absorption spectra for six arrays with distinct periodicities. The vertical arrows indicate the wavelength at which $\lambda/n_{\text{SiO}_2} = P$, marking the onset of first-order diffraction. It can be seen that the absorption is highest in the metamaterials regime (to the right of the vertical arrows), where higher-order diffraction channels are shut off. The right panel in Figure 3d shows spectra of the estimated absorption, as extracted from the reflection and transmission measurements as $A = 1 - R - T_0$. Good qualitative and quantitative agreement is obtained. The higher estimated absorption seen in the measurements on the short wavelength side of the spectrum where $\lambda/n_{\text{SiO}_2} < P$ is linked to some energy loss to light that is redirected in first-order diffracted beams that are not captured by the detector on the transmission side. The simulated absorption quantifies the actual absorption loss inside the film. Minor differences between experiments and simulations are also coming from the not-perfectly rectangular shape of the Ge beams in the experiments. Figure 3e shows the simulated and estimated

absorption at the target wavelength of 600 nm, as extracted from the spectra in 3d. For periods larger than 420 nm, the absorption is low ($\sim 10\%$) due to energy loss into diffracted orders. As the period decreases into the subwavelength range, the absorption rapidly increases with increasing filling fraction of Ge. This is expected as we increase the linear density of absorbing beams. For periods of 250 to 300 nm, the effective index approaches the point of optimal impedance matching and the absorption reaches a maximum close to 50%. It is important to realize that the theoretical maximum absorption for a subwavelength film placed on a quartz substrate is 46.4%, which is lower than for the case of a free-standing metafilm due to the asymmetry in the index of the sub- and superstrates. Because of this fact, the magnitude of the maximum absorption found in the experiment also ends up being a bit lower (43%) than expected from the theory for a free-standing film. Ultimately, the absorption comes down for very small periods where the resonant modes from neighboring beams exhibit a very large degree of overlap and the individual beam resonances disappear. Here the absorption spectrum converges to that of a continuous Ge thin film.

With the demonstrated ability of using optical resonances in high-index nanostructures to tune the effective optical properties of a metafilm, it is worth asking the question what range of optical properties may be achievable. The larger the range of optical properties one can achieve with a single semiconductor material, the greater the flexibility in the design of specific optical functions. Figure 4 shows a map of the effective

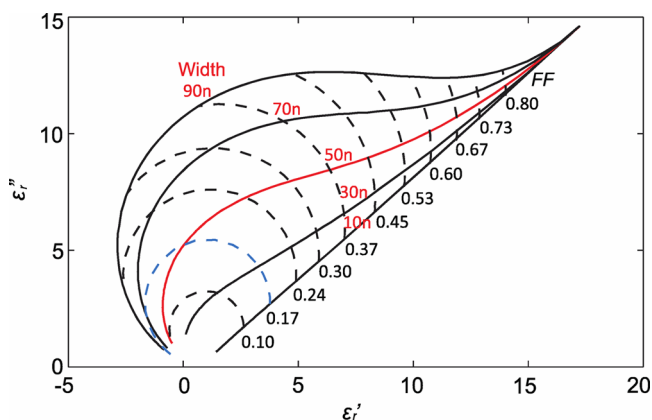


Figure 4. Range of achievable effective optical constants from Ge metafilms under TM illumination. Theoretical boundaries for the effective permittivities at $\lambda = 600$ nm as achievable with resonant and nonresonant Ge nanobeams with a 40 nm height. By varying either the filling fraction at a constant beam width (solid lines) or the beam width at a constant filling fraction (dashed line), a wide range of complex permittivity values can be achieved. The relevant beam widths in nanometer and filling fractions are labeled along the solid and dashed lines. The beam width and filling fraction at which the absorption of a 40 nm thick Ge metafilm are maximized are highlighted in red and blue colors.

permittivities at 600 nm that are achievable by subwavelength patterning of a 40 nm thick semiconductor. By controlling the period and width of the Ge beams, a wide range of permittivity values can be realized. To gain further insight into the way the complex-valued permittivity can be manipulated, we first analyze the evolution of this quantity as we increase the density of beams for different fixed beam widths. Each solid line represents a beam width in the range from 10 to 90 nm. The

boundary of this set of curves indicates the range of achievable permittivities. For the smallest widths, the beams do not support a resonance and an increase in the density causes the permittivity of the metafilm to approach the permittivity of a continuous Ge film along a straight line. This directly follows from first-order effective medium theory. For wider beams that support an electrical dipole resonance (i.e., about 50 nm width), it is the imaginary part of the permittivity that primarily increases as the beams are brought close together. The real part of the permittivity stays small. This can be understood by realizing that on/near resonance, the beams feature a dipolar polarizability $\hat{\alpha}_{\text{NB}} = |\hat{\alpha}_{\text{NB}}|e^{i\theta_d}$ with a phase delay $\theta_d \approx 90^\circ$, that is, $\hat{\alpha}_{\text{NB}}$ is imaginary. At low density, the metafilm's susceptibility is expected to follow in a simple way from the beam's polarizability and the filling fraction of Ge beam-material in a repeating unit cell f_{Ge} as: $\hat{\chi} = f_{\text{Ge}}\hat{\alpha}_{\text{NB}}/\epsilon_0$. With an imaginary $\hat{\alpha}_{\text{NB}}$, one thus expects that the imaginary part of the susceptibility and permittivity will primarily increase with an increasing filling fraction of germanium beam material. As the density of the beams is increased further, the near-field coupling between neighboring beams will increase and ultimately becomes so large that the individual beam resonances disappear. As a result, the permittivity will start converging toward that of a continuous Ge film. For beams that are substantially wider than 50 nm, the real part of the permittivity can even achieve negative values.

The dashed lines in Figure 4 indicate the achievable permittivities that can be obtained by varying the geometrical parameters in a different way. They show the evolution in the effective permittivity of the metafilm as the beam width is varied at a constant filling fraction. At each filling fraction, the increase in beam width causes a rotation in the complex permittivity plane. The blue dashed line at a filling fraction of 0.17 shows the evolution of the permittivity for the beam-array that was discussed in Figure 2. Consistent with Figure 2a, the imaginary part of the permittivity increases upon approaching the beam resonance and then decreases again. At the same time, the real part of the permittivity crosses zero. Figure 4 shows that these changes result in a more-or-less circular path in the complex permittivity plane and an increase in the control of loss angle.

To summarize, we have demonstrated that the ultimate absorption limit for a subwavelength thickness film can be achieved using a semiconductor metafilm. Judiciously designed building blocks, which support optical resonances, can transform the optical properties of a metafilm from that of a semiconductor to an ideal metallic conductor. The key role of the optical resonances is to cause a delay in the phase of the scattered wave from the metafilm. The manipulation of optical resonances enables one to achieve the ultimate absorption limit in a freestanding film as originally predicted for a metal by Wilhelm Woltersdorff.⁹ The general thinking in this paper can also be used to understand the very strong absorption (even strong per unit volume) in deep subwavelength metallic nanostructures.^{27,35} It can also be extended to nanostructured metamaterials supporting both electric and magnetic resonances. For such materials, it was recently suggested that unity absorption can be achieved in an optically thin film (see ref 38 and Supporting Section 1). For all such films, a careful optimization of the scattering amplitude and phase is required to achieve high absorption. More generally, the described metafilm design procedure can be applied to any high index material and enables one to widely tune the optical properties

for a material of interest. This notion breaks open conventional design principles for optoelectronic devices that typically assume that the optical properties of semiconductor materials are intrinsic and fixed.

METHODS

The thin Ge metafilm absorber layers were experimentally defined by e-beam lithography on quartz substrates followed by a-Ge deposition and a lift off process. Measurements of the transmitted and reflected power were made using a confocal optical microscope (Nikon C1) coupled to a CCD camera (Acton Pixis1024, Princeton Instruments) and spectrometer (Acton SP2300i, Princeton Instruments). The experimental estimates of the absorptivities A of the metafilms were obtained from measurements of their reflectivities R and transmittivities T as $A = 1 - R - T_0$. This is a reasonable estimate in the metamaterial regime where no diffracted orders are present. The absorption map of isotropic films for the optimized index point was obtained using the transfer matrix method.³⁹ The numerical analysis of the metafilms was performed based on the finite-difference time-domain (FDTD) method (Lumerical Solutions Inc.). The effective index of the array of resonant building blocks was calculated by tracking the phase and amplitude information on the zeroth order transmitted and reflected waves^{32,33} and making a comparison to values obtained from a scattering matrix formalism.³⁹ The effective index based on the first order effective medium theory for TM polarization ($\hat{\epsilon}_{\text{eff}} = f_1 \hat{\epsilon}_1 + (1 - f_1) \hat{\epsilon}_2$) and TE polarization ($\hat{\epsilon}_{\text{eff}} = 1 / [f_1 / \hat{\epsilon}_1 + (1 - f_1) / \hat{\epsilon}_2]$) are compared in the Supporting Information S2 for completeness. The absorption by the metafilms was evaluated by calculating the Ohmic absorption ($0.5 \cdot \omega \cdot \epsilon_0 \text{Im}(\hat{\epsilon}_r) \cdot |\hat{E}|^2$) in the individual beams.

ASSOCIATED CONTENT

Supporting Information

The Supporting Information is available free of charge on the ACS Publications website at DOI: 10.1021/acs.nanolett.6b01198.

Analysis on the ultimate limit for 50% light absorption in free-standing, ultrathin film and polarization dependence of the effective permittivity. (PDF)

AUTHOR INFORMATION

Corresponding Author

*E-mail: brongersma@stanford.edu.

Author Contributions

The manuscript was written through contributions of all authors. All authors have given approval to the final version of the manuscript.

Notes

The authors declare no competing financial interest.

ACKNOWLEDGMENTS

This work was supported by the "Light-Material Interactions in Energy Conversion" Energy Frontier Research Center funded by the U.S. Department of Energy, Office of Science, Office of Basic Energy Sciences under Award Number DE-SC0001293. Part of this work was also funded by AFOSR Grant Number FA9550-14-1-0117.

REFERENCES

- (1) Atwater, H. A.; Polman, A. *Nat. Mater.* **2010**, *9*, 865–865.
- (2) Brongersma, M. L.; Cui, Y.; Fan, S. *Nat. Mater.* **2014**, *13*, 451–460.
- (3) Ferry, V.; Verschuuren, M. A.; van Lare, M. C.; Schropp, R. E. I.; Atwater, H. A.; Polman, A. *Nano Lett.* **2011**, *11*, 4239–4245.
- (4) Kim, S. J.; Thomann, I.; Park, J.; Kang, J. – H.; Vasudev, A.; Brongersma, M. L. *Nano Lett.* **2014**, *14*, 1446–1452.
- (5) Liu, C.-H.; Chang, Y.-C.; Norris, T. B.; Zhong, Z. *Nat. Nanotechnol.* **2014**, *9*, 273–278.
- (6) Baugher, B. W. H.; Churchill, H. O. H.; Yang, Y.; Jarillo-Herrero, P. *Nat. Nanotechnol.* **2014**, *9*, 262–267.
- (7) Biener, G.; Niv, A.; Kleiner, V.; Hasman, E. *Opt. Lett.* **2007**, *32*, 994–996.
- (8) Rephaeli, E.; Fan, S. *Opt. Express* **2009**, *17*, 15145–15159.
- (9) Woltersdorff, W. *Eur. Phys. J. A* **1934**, *91*, 230–252.
- (10) Dallenbach, W.; Kleinsteuber, W. *Hochfrequenztechnik und Elektroakustik* **1938**, *51*, 152.
- (11) Woo, J. M.; Kim, M. S.; Kim, H. W.; Jang, J. H. *Appl. Phys. Lett.* **2014**, *104*, 081106.
- (12) Salisbury, W. W. US Patent No. 2,599,944, 1952.
- (13) Fante, R. L.; McCormack, M. T. *IEEE Trans. Antennas Propag.* **1988**, *36*, 1443–1454.
- (14) Razansky, D.; Einziger, P. D.; Adam, D. R. *Phys. Rev. Lett.* **2004**, *93*, 083902.
- (15) Bosman, H.; Lau, Y. Y.; Gilgenbach, R. M. *Appl. Phys. Lett.* **2003**, *82*, 1353–1355.
- (16) Jackson, J. D. *Classical Electrodynamics*, 3rd ed.; Wiley: New York, 1998.
- (17) Smith, D. R.; Pendry, J. B.; Wiltshire, M. C. K. *Science* **2004**, *305*, 788–792.
- (18) Kildishev, A. V.; Boltasseva, A.; Shalae, V. M. *Science* **2013**, *339*, 1232009.
- (19) Landy, N.; Sajuyigbe, S.; Mock, J.; Smith, D.; Padilla, W. *Phys. Rev. Lett.* **2008**, *100*, 207402.
- (20) McVay, J.; Hoorfar, A.; Engheta, N. *Microw. Opt. Technol. Lett.* **2009**, *51*, 785–790.
- (21) Aspnes, D. E. *Am. J. Phys.* **1982**, *50*, 704–709.
- (22) Stephens, R.; Cody, G. *Thin Solid Films* **1977**, *45*, 19–29.
- (23) Lalanne, P.; Hutley, M. *Encycl. Opt. Eng.* **2003**, 62–71.
- (24) Häggglund, C.; Apell, S. P.; Kasemo, B. *Nano Lett.* **2010**, *10*, 3135–3141.
- (25) Häggglund, C.; Apell, S. P. *J. Phys. Chem. Lett.* **2012**, *3*, 1275–1285.
- (26) Aydin, K.; Ferry, V. E.; Briggs, R. M.; Atwater, H. A. *Nat. Commun.* **2011**, *2*, 517.
- (27) Häggglund, C.; Zeltzer, G.; Ruiz, R.; Thomann, I.; Lee, H. -B. -R.; Brongersma, M. L.; Bent, S. F. *Nano Lett.* **2013**, *13*, 3352.
- (28) Shen, J. T.; Catrysse, P. B.; Fan, S. *Phys. Rev. Lett.* **2005**, *94*, 197401.
- (29) Jung, J.; Martín-Moreno, L.; García-Vidal, F. J. *New J. Phys.* **2009**, *11*, 123013.
- (30) Cao, L.; Park, J.-S.; Fan, P.; Clemens, B.; Brongersma, M. L. *Nano Lett.* **2010**, *10*, 1229–33.
- (31) Cao, L.; Fan, P.; Vasudev, A. P.; White, J. S.; Yu, Z.; Cai, W.; Schuller, J.; Fan, S.; Brongersma, M. L. *Nano Lett.* **2010**, *10*, 439–445.
- (32) Smith, D. R.; Vier, D. C.; Koschny, T.; Soukoulis, C. M. *Phys. Rev. E* **2005**, *71*, 036617.
- (33) Smith, D. R.; Schultz, S.; Markoš, P.; Soukoulis, C. M. *Phys. Rev. B: Condens. Matter Mater. Phys.* **2002**, *65*, 195104.
- (34) Pardo, F.; Bouchon, P.; Haidar, R.; Pelouard, J.-L. *Phys. Rev. Lett.* **2011**, *107*, 093902.
- (35) Luk'yanchuk, B. S.; Miroshnichenko, A. E.; Tribelsky, M. I.; Kivshar, Y. S.; Khokhlov, A. R. *New J. Phys.* **2012**, *14*, 093022.
- (36) Bohren, C. F.; Huffman, D. R. *Absorption and Scattering of Light by Small Particles*; Wiley: New York, 1998; pp227–267.
- (37) Huang, K.; Jun, Y. C.; Seo, M. – K.; Brongersma, M. L. *Opt. Express* **2011**, *19*, 19084.

- (38) Ra'di, Y.; Simovski, C. R.; Tretyakov, S. A. *Phys. Rev. Appl.* **2015**, *3*, 037001.
- (39) Pettersson, L. A. A.; Roman, L. S.; Inganas, O. J. *Appl. Phys.* **1999**, *86*, 487.